JCRS

Journal of Chemical Reactivity and Synthesis 2021: 11(2) 62-90

Research Article

A computational study of N_2 adsorption on aromatic metal Mg16M;(M=Be, Mg, and Ca) nanoclusters

Mahmood Reza Dehghan, Sara Ahmadi*

Department of Chemistry, Firoozabad Branch, Islamic Azad University, Firoozabad, Iran.

ARTICLE INFO:

Received:
19 March 2021

Accepted:
26 April 2021

Available online:
12 June 2021

✉: S. Ahmadi
Saraahmadi1380@yahoo.com

ABSTRACT

Metal nanoclusters have been considered as a new class of chemical sensors due to their unique electronic structures and the particular physicochemical properties. The interaction of N2 molecule with neutral and ionic magnesium nanoclusters ⟦Mg⟧_17^q (q=0,±1), as well as neutral magnesium nanoclusters with the centrality of beryllium and calcium Mg16M (M=Be, Mg, and Ca) have been investigated using CAM-B3LYP/6-311+G(d) level of theory in the gas phase. The electronic properties of magnesium nanoclusters were significantly affected by the adsorption of N2 molecule. The NBO analysis revealed a charge transfer from the adsorbed N2 molecule to the nanocluster. Based on the adsorption energies and enthalpies, a thermodynamically favorable chemisorption process was predicted for the Mg16Ca—N2 complex. The negative value of the Gibbs free energy of Mg16Ca—N2 confirmed the spontaneous adsorption process. The estimated recovery time for Mg16Ca—N2 complex for 8-MR (0.089 s) and 4-MRs (0.075 s) illustrated a possible desorption process for N2 molecule from the surface of Mg16Ca. Our finding also revealed the Mg16Ca has the ability to use as a sensor for detection and absorption of N2 molecule.

Keywords: Magnesium nanocluster, Adsorption, Nitrogen, Sensor, Electronic properties, DFT

1. Introduction

Nitrogen gas, which makes up 78% of the Earth's atmosphere, is the most plentiful element in the Earth [1]. The nitrogen gas has different applications such as the ammonia production in the Haber process, the net gas in explosive liquid tanks [2], diodes [3], and stainless metals production [4]. It can be used as a refrigerant in the cryogenic cooling and storage systems in the food and pharmaceutical. It is a key element in the cells of living organisms [5]. Expensive experimental techniques such as spectrophotometry [6], electrochemistry [7], and chromatography [8] are used for the detection of N_2. Hence, it is of great importance to find a portable, fast, and sensitive sensor for detection and adsorption of nitrogen gas. With the advent of nanotechnology, the development of high capacity sensors with high surface to volume ratio and special electronic sensitivity is on the rise [9]. A new class of sensors such as nanoclusters has been broadly considered as chemical sensors [10, 11]. For this purpose, metal nanoclusters are promising candidates.

Metal nanoclusters are a kind of nanoscale size particle with unusual properties that behave quite differently from macroscopic metals. A nanocluster behaves like a molecule and known as the bridging link between atoms and nanoparticles. These metal nanoclusters were known as unparalleled properties materials with unique behavior such as size and number of atoms. These materials have been studied by many researchers due to their biocompatibility metals properties and featuring significant metal-metal interactions [12-16]. Divalent metal

nanoclusters with filled electronic layers represent the special aspects of van der Waals bonding between the atoms. These behaviors significantly differ from the behavior of a single atom or bulky materials [17]. Among the divalent metal nanoclusters, magnesium nanoclusters received great attention in the last twenty years due to interesting properties such as stability in the high temperature, low dielectric constant, high thermal conductivity, intense chemical reactivity, and oxidation resistance [18-21]. The diatomic molecule of magnesium is a weakly bonded van der Waals system, but magnesium nanoclusters of larger sizes represent strong bonding [17]. These properties of magnesium were led to several applications such as superconductivity [22], hydrogen storage [23, 24], nano-materials [25, 26], and biomedical [27]. Besides these remarkable properties, transition van der Waals bonding to metallic bonding was observed in magnesium nanoclusters with increasing the cluster size [28].

The structural and electronic properties of magnesium nanoclusters have been investigated using several theoretical methods [29-33]. Xia and coworkers studied the structural evolution and electronic properties of the neutral and anionic *Mg* clusters with a different number of atoms from 3 to 20 using the unbiased CALYPSO method combined with density functional theory [33]. They demonstrated that the most stable neutral clusters are consisting of 17 atoms, includes two square frames (4-MRs) on the top and down with an octagon frame (8-MR) at the center (Figure. 1), which has been considered as an aromatic metal cluster. Jellinek *et al.* investigated the structural and electronic properties of neutral and anionic magnesium clusters up to 22 atoms using gradient-corrected density functional theory [34]. Lyalin *et al.* have studied the evolution of the optimized structures of the neutral and singly charged cationic magnesium clusters with increasing the cluster size by ab initio method systematically [35]. Nitrogen adsorption on various nanostructures has been extensively investigated theoretically and experimentally [36-39]. The goal of this study is to examine the

possibility of N_2 adsorption on the surface of the magnesium nanoclusters consisting of 17 atoms with the centrality of *Be*, *Mg*, and *Ca* (Figure. 1), and also on the ionic structure of $Mg_{17}^{q}(q=0,\pm1)$ in the gas phase using density functional theory (DFT) calculations. DFT is the most precise and reliable method to investigate the metal clusters properties [40-45]. The natural bond orbital (NBO) analysis [46] was used to interpret the charge transfer process between N_2 molecule and $Mg_{16}M$;(*M=Be, Mg,* and, *Ca*) and also ionic nanoclusters during the adsorption process.

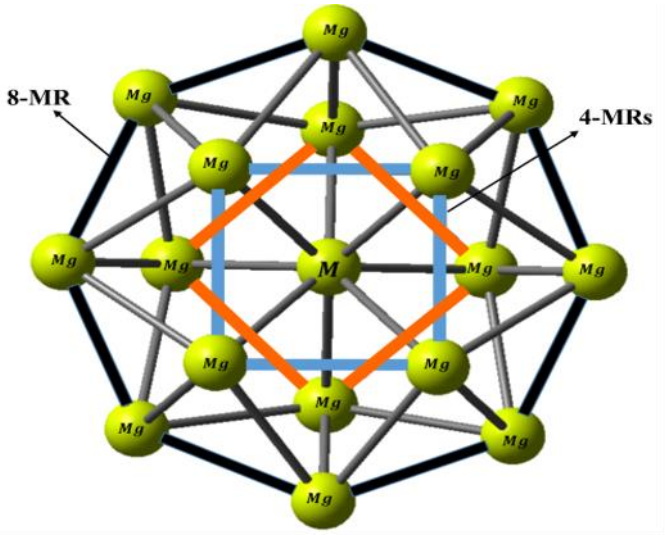

Figure. 1 Schematic view of the Mg_{17} nanoclusters, the blue and red bonds represent the two 4-membered rings (4-MRs) and the thick black bonds represent one 8-membered ring (8-MR), M is the central atom (*M=Be, Mg,* and *Ca*).

2. Theoretical Methods

The initial structure of N_2 molecule, the $Mg_{17}^{q}(q=0,\pm1)$ and the $Mg_{16}M$;(*M=Be, Mg,* and, *Ca*) nanoclusters were modeled using Gauss View 5.0 [47]. A filled-cage-like construction, including two square (4-MRs) frames and an octagon (8-MR) frame was applied to stabilize the $Mg_{16}M$ due to the potent interactions between the Mg_4 units and the central *M* atom;(*M=Be, Mg,* and, *Ca*) and more significantly because of the tendency of local aromaticity [33]. A single N_2 molecule was geometry optimized separately and added to each

of these nanoclusters from two different sites of 4-MRs and 8-MR (Figure. 1). All structures were geometrically optimized using the hybrid exchange-correlation functional CAM-B3LYP [48]. The CAM-B3LYP is a good functional for energetic studies and structural parameters and predicts the energetic quantities to the accuracy of B3LYP [49]. It has also a high accuracy resulting in long-range correction effect [48]. To reduce the calculation time, the geometry optimizations have been started with 6-31+G followed by a higher precision basis set (6-311+G(d)) to extract the energetic values in the gas phase using the Gaussian 09 software package [50]. Normal mode frequency analysis was performed numerically from the analytical gradients. The absence of negative frequency in normal mode analysis indicates the optimized structure on the potential energy surfaces (PES) were real minimum stationary points. The adsorption energies of the studied complexes are corrected separately, for both zero point energy (ZPE) and basis set superposition error (BSSE) using the counterpoise correction scheme outlined by Boys and Bernardi [51]. Furthermore, using the obtained results from the calculations, the structural and electronic properties and also the thermodynamic parameters were calculated. The density of state (DOS), partial density of state (PDOS) and total density of state (TDOS) plots were obtained for all adsorption models using the Gauss Sum [52] and Multiwfn [53] programs. The EDD maps were generated by VMD software.

3. Results and discussions

3.1 Geometry optimization and validation

The neutral Mg_{17} nanocluster with D_{4d} point group is the most stable among other point groups such as C_s, D_{17h}, and, $D_{\infty h}$[21, 33]. The structure of the nitrogen molecule, the ionic forms of Mg_{17}^{q} $(q = \pm 1)$ and also the neutral $Mg_{16}M$;(*M=Be*, *Mg*, and, *Ca*) nanoclusters were geometry optimized at the CAM-B3LYP/6-311+G(d) level of theory in the gas phase

separately (Figure. SF1, supplementary material) and the bond lengths and angles are tabulated in Tables ST1-7, supplementary material. Table 1 summarizes the calculated bond lengths and angles of $Mg_{17}^{q}(q=0,\pm1)$ and $Mg_{16}M$;(*M=Be, Mg,* and, *Ca*) nanoclusters for 8-MR and 4-MRs frames. The obtained results fall within the range of corresponding values reported in experimental studies Ref [54] and theoretical works in Ref [55]. Table ST8, supplementary material, illustrates the calculated bond length of *Mg—Mg* and the total energy of Mg_{17} nanocluster with CAM-B3LYP/6-311+G(d) for Mg_{17} nanocluster and compares with those from theoretical reported values [21]. There is good agreement between our results and those from B3LYP/6-311G(d) and B3PW91/6-311G(d). According to Table 1 accepting or losing an electron directly influences the bond lengths and angles of the nanoclusters. Therefore, the bond lengths and angles of 4-MRs and 8-RM frames of Mg_{17}^{+1}, and Mg_{17}^{-1} slightly change in comparison to the neutral Mg_{17} nanocluster. As an example, the bond angles for 8-MR frame of Mg_{17}, Mg_{17}^{-1}, and Mg_{17}^{+1} are 116.39°, 114.85°, and 116.91° respectively, but for 4-MRs frames, it is equal to 89.97°, 89.99°, and 90.01° respectively. Therefore, the Mg_{17}^{-1} with the average bond length of 3.02 ± 0.01Å and bond angle of 114.85° for 8-MR frame and 3.04 ± 0.02 Å and 89.97° for 4-MR frame is less stable in comparison to the Mg_{17} and Mg_{17}^{+1}, which could be related to the reduction of the bond length and angles in the anionic nanocluster.

Table 1. The average bond lengths in (Å) and bond angles in (°) of $Mg_{17}^{q}(q=0,\pm1)$ and $Mg_{16}M$;(*M=Be, Mg,* and, *Ca*) nanoclusters in 4-MRs and 8-RM frames.

Nanoclusters	Metal ring frame	Bond length	Bond angle
Mg_{17}^{-1}		3.02 ± 0.01	114.85
Mg_{17}^{+1}	8-MR	3.02 ± 0.02	116.91

Mg_{17}^{-1}	4-MRs	3.04 ± 0.02	89.97
Mg_{17}^{+1}		3.11 ± 0.01	89.99
$Mg_{16}Be$	8-MR	3.12 ± 0.01	115.44
Mg_{17}		3.04 ± 0.01	116.39
$Mg_{16}Ca$		2.95 ± 0.01	112.76
$Mg_{16}Be$	4-MRs	2.92 ± 0.01	89.99
Mg_{17}		3.05 ± 0.01	90.01
$Mg_{16}Ca$		3.27 ± 0.01	89.91

Table 1 also exhibits that the bond lengths and angles in $Mg_{16}M$;(*M=Be, Mg,* and, *Ca*) nanoclusters are affected by the central atom (*M*) in both 4-MRs and 8-MR frames. As such, the bond lengths for 4-MRs frames of $Mg_{16}M$ increased with increasing the size of the central atom whilst, for the 8-MR frame the bond lengths show an inverse trend. The bond angle for 8-MR frame, in $Mg_{16}Ca$ is 112.76˚, which is smaller than the values of $Mg_{16}Be$ and Mg_{17}, consequently, leading to the cluster instability. It can be concluded that the 8-MR frame of $Mg_{16}Ca$ with the smallest bond length (2.95 Å) and angle (112.76˚) and high strain ring is the most favorable position of nanocluster for adsorbing N_2 molecule. This result is in agreement with the obtained results of the adsorption energy values in the 3.2 section.

3.2 Adsorption behavior of N_2 molecule on the $Mg_{16}M$ nanoclusters

The interaction energies of the $Mg_{16}Be$—N_2, Mg_{17}—N_2 , $Mg_{16}Ca$—N_2 and also the Mg_{17}^{+1}—N_2 and Mg_{17}^{-1}—N_2 complexes were calculated to determine the adsorption behavior of N_2 molecule upon the exterior surface of the $Mg_{16}M$;(*M=Be, Mg,* and, *Ca*) nanoclusters. The adsorption energy (E_{ad}), binding energy (E_{bind}) and deformation energy (E_{def}) are calculated based on following equations:

$$Mg_{16}M^{q} + N_2 \rightarrow Mg_{16}M^{q} \ldots N_2 \qquad M = (Be, Mg, Ca) \qquad (q = 0, \pm 1)$$

$$E_{ad} = E_{Mg_{16}M^{q}\ldots N_2} - (E_{Mg_{16}M^{q}} + E_{N_2}) \quad (1)$$

$$E_{bind} = E_{Mg_{16}M^{q}\ldots N_2} - (E_{Mg_{16}M^{q}\ in\ complex} + E_{N_2\ in\ complex}) \quad (2)$$

$$E_{def} = E_{ad} - E_{bind} \quad (3)$$

where $E_{Mg_{16}M^{q}\ldots N_2}$, $E_{Mg_{16}M^{q}}$, and E_{N_2} are the optimized energies of the complex (nanocluster/N_2), nanocluster and N_2 molecule, respectively. It should be mentioned that the adsorption energy encompasses both binding (E_{bind}) and deformation (E_{def}) energy contributions, which are both occurred during the adsorption process [56].

Table 2 displays the values of the adsorption (E_{ad}) and interaction (E_{bind}) energies with the correction of the basis set superposition errors (BSSE), and deformation energies (E_{def}) for N_2 adsorption on the surface of the $Mg_{16}M$;(*M=Be, Mg,* and, *Ca*) nanoclusters. The adsorption energy values of the 4-MRs and 8-MR frames for $Mg_{16}Be$—N_2, Mg_{17}—N_2, and $Mg_{16}Ca$—N_2 complexes are (-1.0915, -4.6333); (-1.3698, -0.8128); and (-88.0620, -87.6170) (kJ.mol^{-1}) respectively. It is clear that the $Mg_{16}Ca$— N_2 complex has the highest adsorption energy. This indicates a strong interaction between N_2 molecule and $Mg_{16}Ca$ nanocluster which shows a chemisorption process. Whilst, the values of the adsorption energies for the other complexes indicate the N_2 molecule adsorbs physically upon the surface of the investigated nanoclusters.

Table 2. The calculated basis set superposition errors (δ_{BSSE}), adsorption (E_{ad}), binding (E_{bind}) and deformation (E_{def}) energies (all in kJ.mol^{-1}) of $Mg_{16}M{-}N_2$;(*M=Be, Mg,* and, *Ca*) and $Mg_{17}^{q}(q = \pm 1)$ complexes with the BSSE correction, at the CAM-B3LYP/6-311+G (d) approach.

Complexes	Metal ring frame	δ_{BSSE}	$E_{ad} + BSSE$	$E_{bind} + BSSE$	E_{def}
Mg_{17}^{-1}—N_2		0.0021	-0.8857	-199.1755	+198.2898
Mg_{17}^{+1}—N_2	8 –MR	0.0247	-6.8629	-1555.6449	+1548.7819
$Mg_{16}Be$—N_2		0.0186	-4.6333	-1.6073	-3.0260

Mg_{17}—N_2		0.0020	-0.8128	-1.0038	+0.1910
$Mg_{16}Ca$—N_2		0.0351	-87.6170	-1.7789	-85.8381
Mg_{17}^{-1}—N_2		0.0018	-0.1711	-197.1642	+196.9931
Mg_{17}^{+1}—N_2		0.0176	-7.5697	-1556.6062	+1549.0365
$Mg_{16}Be$—N_2	4-MRs	0.0016	-1.0915	-1.0246	-0.0669
Mg_{17}—N_2		0.0014	-1.3698	-1.5488	+0.1790
$Mg_{16}Ca$—N_2		0.0425	-88.0620	-1.1240	-86.9380

According to section 3.3, the stability of the neutral $Mg_{16}M$;(*M=Be, Mg,* and, *Ca*) nanoclusters will decrease with increasing the central atom radius, which leads to more reactivity. Accordingly, the $Mg_{16}Ca$ has the highest adsorption energy for the nitrogen molecule. It should be noted that the electronegativity of the central atom can be an important factor during the nitrogen adsorptions on the investigated nanoclusters. Hence, calcium with the least electronegativity plays a more effective role in nitrogen adsorption.

The adsorption energy values of Mg_{17}—N_2, Mg_{17}^{+1}—N_2 and Mg_{17}^{-1}—N_2 complexes for 8-MR and 4-MRs frames are (-0.8128, -1.3698); (-6.8629, -7.5697); and (-0.8857, -0.1711) (kJ.mol^{-1}), respectively. The comparison of the adsorption energy values of N_2 molecule over the studied nanoclusters reveals that the substitution of the central atom of the nanocluster is more effective than the charge alteration. Therefore, the adsorption energy values of $Mg_{16}Ca$—N_2 complex from both positions of 4-MRs and 8-MR frames are more than the related values of the other neutral and anionic complexes. The values of the adsorption energies for the $Mg_{17}^{q}(q=0,\pm1)$ complexes indicate the N_2 molecule adsorbs physically on the surface of the investigated clusters.

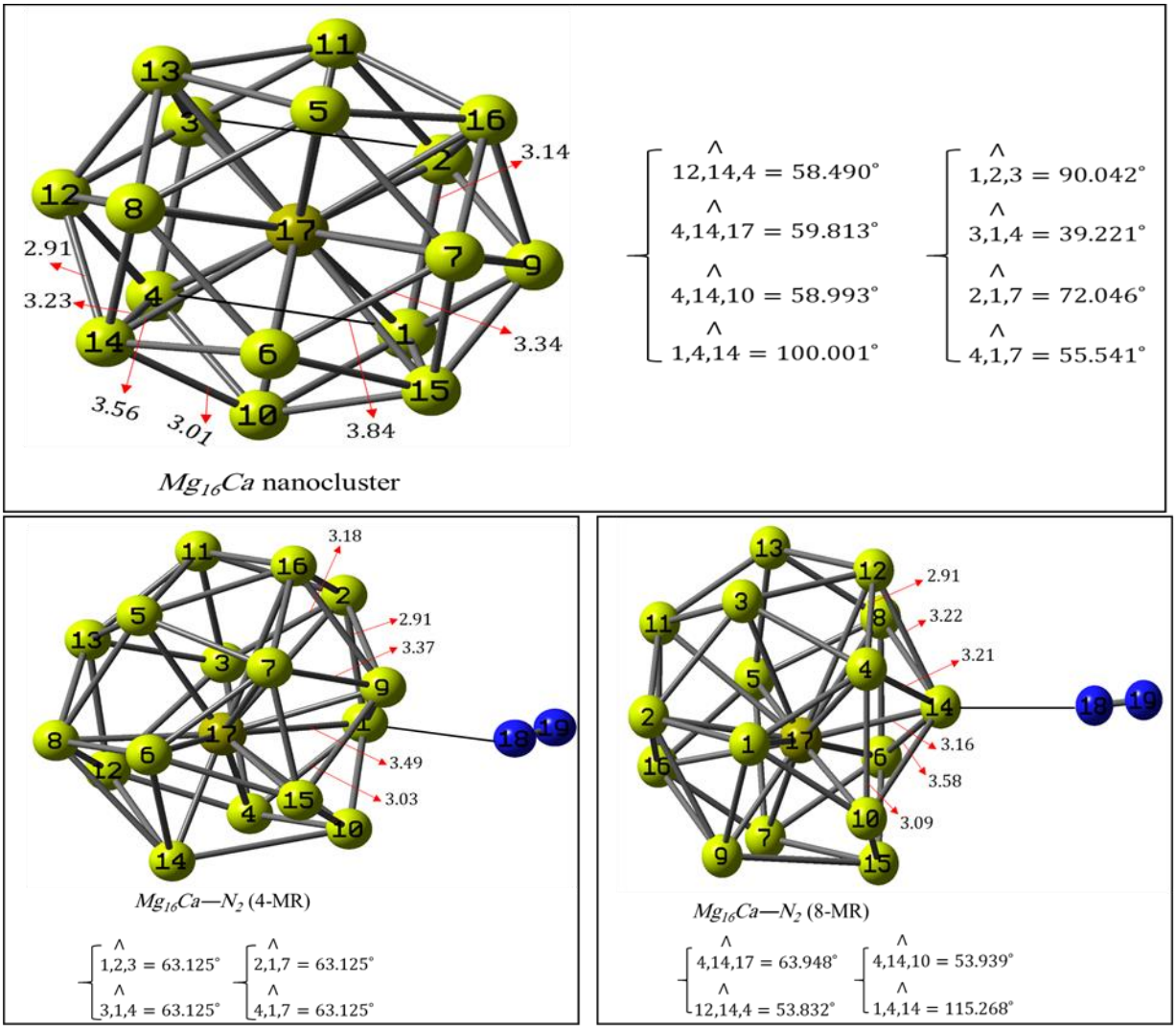

Figure. 2 Comparison of the bond lengths and angles of $Mg_{16}Ca$ nanocluster before and after N_2 adsorption. All bond distances are in Å.

The deformation energy values of the neutral, cationic, and anionic $Mg_{17}^{q}—N_2$ $(q = 0, \pm 1)$ nanoclusters are positive which indicate an endothermic-unfavorable adsorption process of N_2 molecule upon the surface of $Mg_{17}^{q}(q = 0, \pm 1)$ whilst, the negative deformation energies for $Mg_{16}Be$ and $Mg_{16}Ca$, implying an exothermic-favorable adsorption process. Hence, for $Mg_{16}Be$ and $Mg_{16}Ca$ nanoclusters, the adsorption process is thermodynamically spontaneous and lead to a distortion in the nanocluster structure. Figure. 2 illustrates that the $Mg_{16}Ca—N_2$ with the largest deformation energy values of (4-MRs= -86.938 kJ.mol^{-1} and 8-

MR= -85.838 kJ.mol^{-1}) shows dramatic changes in the bond lengths and angles of $Mg_{16}Ca$ after the N_2 adsorption. The charge transfer between the N_2 molecule and different nanoclusters were analyzed using the natural bond orbital (NBO) technique. Figure. 3 displays a high charge transfer (0.07110 e) during the adsorption of N_2 molecule on the 8-MR frame of $Mg_{16}Ca$ nanocluster, which motivates the highest interaction energy among the adsorption models ($Mg_{16}M$;(*M=Be, Mg,* and, *Ca*). On the other hand, the natural bond orbitals (NBO) analysis indicates that a remarkable charge (Figure. 3) is transferred from the N_2 to the $Mg_{16}Ca$ nanocluster which is responsible for the large change of the electronic properties. By decreasing the curvature of the $Mg_{16}M$;(*M=Be, Mg,* and, *Ca*) nanoclusters, the charge transfer is decreased which is in agreement with the reduction of sensitivity and adsorption energy (see Table 2 and Figure. 3) [57-59]. The calculated NBO charges for the neutral and ionic nanoclusters of Mg_{17}^{q} $(q = 0, \pm 1)$ represent the most accumulation of negative charge on the central atom (Table ST9, supplementary material). The charge transfer from N_2 molecule to the Mg_{17}^{-1} nanocluster causes a weak interaction compared to the cationic nanoclusters which can be attributed to the electronic repulsion between the N_2 molecule and the anionic nanocluster. The electron density depletion (EDD) map analysis represents condense electronic cloud surrounded the *Mg—N* bond, which is an evidence for the adsorption of N_2 molecule on the neutral and ionic nanoclusters (Figures 3 and SF2-SF4, supplementary material).

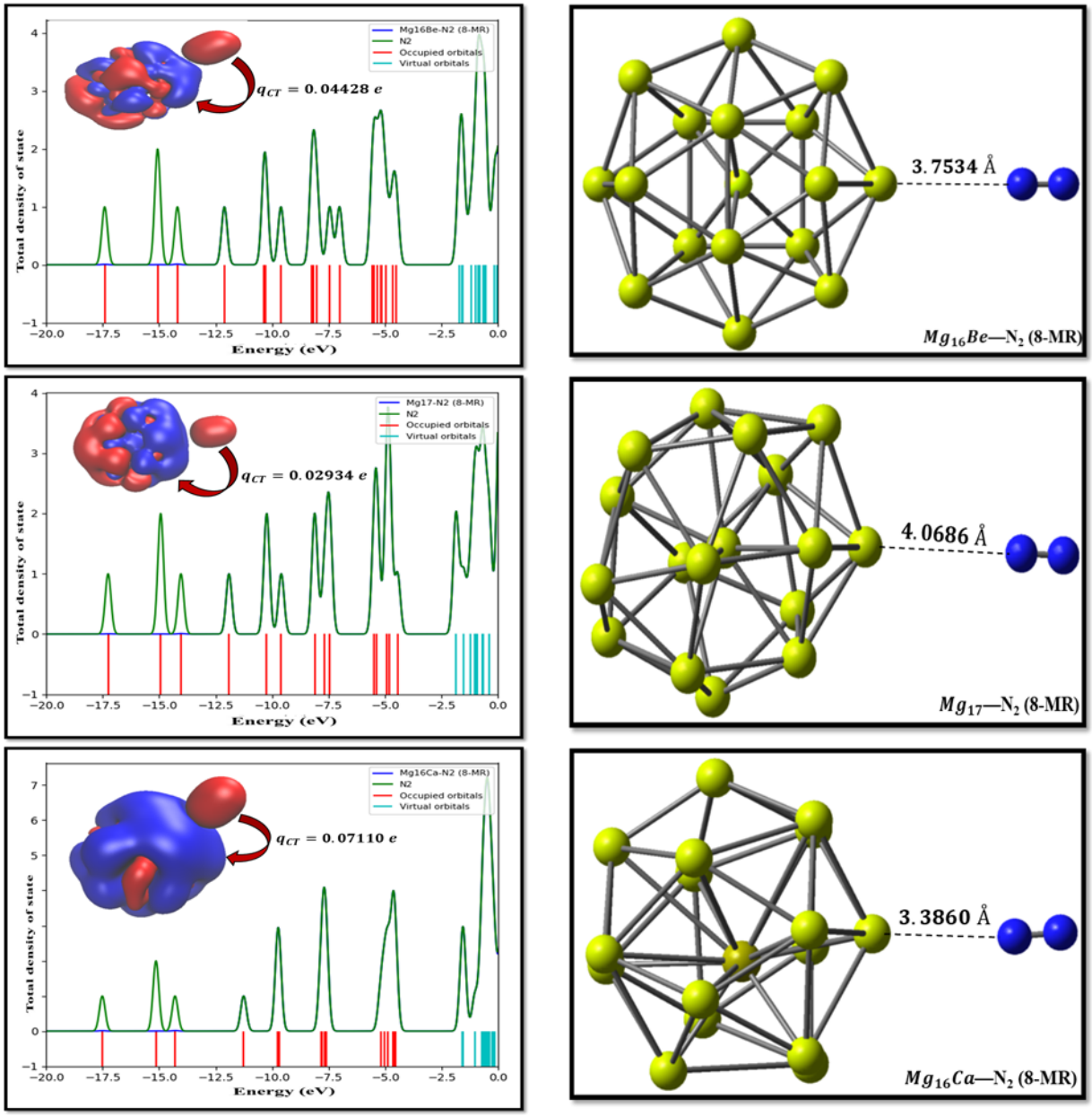

Figure. 3 The optimized structures of the adsorbed nitrogen over the $Mg_{16}M$;(*M=Be, Mg,* and, *Ca*) nanocluster from 8-MR position along with their corresponding electron density depletion (EDD) maps (0.001 au) and PDOS plots. In the EDD maps, the electron density depletion and accumulation sites are displayed in red and blue, respectively. All bond distances are in Å. q_{CT} indicates the charge transfer.

Although the electronic properties of the $Mg_{16}M$;(*M=Be, Mg,* and, *Ca*) nanoclusters are sensitive to N_2 molecule, the high adsorption energy can prevent the desorption process. Exposing to ultraviolet (UV) light [60] can use to recover a sensor experimentally. The recovery time (τ) can be determined using equation (4) based on the the transition theory:

$$\tau = \upsilon^{-1}\exp(-E_{ad}/kT) \quad (4)$$

where T is the temperature, k is the Boltzmann's constant ($\sim 8.31 \times 10^{-3}\ kJ/mol.K$), and υ is the attempt frequency. In order to study this issue in more detail, the recovery time was calculated and computed results tabulated in Table 3. If the vacuum UV light ($\upsilon \sim 3 \times 10^{16}\ s^{-1}$) is applied for the recovery of N_2 molecule from the surface of the most stable ($Mg_{16}Ca$—N_2) complex, the recovery time at 298 K will be about 0.075 s for 4-MRs frames and 0.089 s for 8-MR frame. The estimated recovery time represents a possible desorption process of N_2 molecule from the surface of the $Mg_{16}Ca$ nanocluster. Hence the $Mg_{16}Ca$ nanocluster could be an appropriate sensor for N_2 molecule in comparison to $Mg_{16}Be$ and Mg_{17} nanoclusters.

Table 3. The estimated recovery time (τ) in (s) for the studied complexes.

Metal ring frame	Mg_{17}^{-1}—N_2	Mg_{17}^{+1}—N_2	$Mg_{16}Be$—N_2	Mg_{17}—N_2	$Mg_{16}Ca$—N_2
8-MR	4.76×10^{-17}	5.32×10^{-16}	2.16×10^{-16}	4.62×10^{-17}	0.075
4-MRs	3.57×10^{-17}	7.08×10^{-16}	5.17×10^{-17}	5.79×10^{-17}	0.089

3.3 Electronic properties

The remarkable contribution in the chemical stability and chemical reactivity is related to the frontier orbitals of the highest occupied molecular orbital energies (HOMO) and lowest unoccupied molecular orbital energies (LUMO) which illustrate the electron-donating and accepting ability, respectively [61]. The evaluation of the transition energy from HOMO to LUMO (energy gap; E_{gap}) was carried out to measure the molecular reactivity and evaluation of the sensitivity of each nanocluster relative to N_2 molecule. Table 4 illustrates the values of the highest occupied molecular orbital energies (ε_{HOMO}) and the lowest unoccupied molecular

orbital energies (ε_{LUMO}), energy gap (E_{gap}), chemical potential (μ), chemical hardness (η) and, electronegativity (χ) for the studied complexes.

Comparing the ε_{HOMO} and ε_{LUMO} of the $Mg_{16}Ca$ nanocluster with the $Mg_{16}Ca$— N_2 complex during the adsorption process indicated that the ε_{HOMO} of the $Mg_{16}Ca$ nanocluster was decreased from -4.0518 to -4.5525 eV and -4.5486 eV for the 8-MR and 4-RMs frames, respectively. Whilst, the ε_{LUMO} of the $Mg_{16}Ca$ nanocluster was increased from -2.1034 to -1.5764 eV and -1.5809 eV for 8-MR and 4-MRs frames, respectively. On the other hand, the $\Delta E_{gap}\%$ (the percentage of the nanoclusters bandgap changes during the adsorption of N_2 molecule) has large values for 8-MR (i.e; +52.7458%) and 4-MRs frames (i.e; +52.3147%) of the $Mg_{16}Ca$ nanocluster. Accordingly, the HOMO and LUMO energy levels for the $Mg_{16}Ca$ nanocluster is significantly affected by the adsorption of N_2 molecule. The ε_{HOMO} and ε_{LUMO} values for 4-MRs and 8-MR frames of the other complexes were increased during the adsorption process.

Table 4. The energy of HOMO (ε_{HOMO}), LUMO (ε_{LUMO}), gap energies (E_{gap}), chemical potential (μ), chemical hardness (η), and electronegativity (χ) (all in eV) for the studied compounds, at the CAM-B3LYP/6-311+G (d) approach.

structure		ε_{HOMO}	ε_{LUMO}	E_{gap}	$\Delta E_{gap}\%$	μ	η	χ
N_2		-13.9254	+0.5954	+14.5208	—	-6.6650	+7.2604	+6.6650
$Mg_{16}Be$		-4.6749	-1.6572	+3.0177	—	-3.1682	+1.5089	+3.1682
Mg_{17}		-4.4599	-1.8639	+2.5960	—	-3.1633	+1.2981	+3.1633
$Mg_{17}^{+1^{*}}$		-7.3463	-4.5560	+2.7903	—	-5.9511	+1.3951	+5.9511
$Mg_{17}^{+1^{**}}$		-7.5392	-4.8102	+2.7290	—	-6.1747	+1.3645	+6.1747
$Mg_{17}^{-1^{*}}$		-1.6833	+0.6158	+2.2991	—	-0.5337	+1.1495	+0.5337
$Mg_{17}^{-1^{**}}$		-1.8071	+0.6596	+2.4667	—	-0.5737	+1.2333	+0.5737
$Mg_{16}Ca$		-4.0518	-2.1034	+1.9484	—	-3.0801	+0.9742	+3.0801
$Mg_{16}Be$—N_2	(8-MR)	-4.4904	-1.7146	+2.7758	-8.0160	-3.1025	+1.3879	+3.1025
	(4-MRs)	-4.6681	-1.6511	+3.0170	-0.0232	-3.1596	+1.5085	+3.1596
Mg_{17}— N_2	(8-MR)	-4.4417	-1.8482	+2.5935	-0.0963	-3.1449	+1.2968	+3.1449
	(4-MRs)	-4.4387	-1.8523	+2.5864	-0.3698	-3.1455	+1.2932	+3.1455
$^{*}Mg_{17}^{+1}$— N_2	(8-MR)	-7.2358	-4.4774	+2.7584	-1.1432	-5.8566	+1.3792	+5.8566
	(4-MRs)	-7.2526	-4.4365	+2.8161	+0.9246	-5.8446	+1.4080	+5.8446
$^{**}Mg_{17}^{+1}$— N_2	(8-MR)	-7.4448	-4.6376	+2.8072	+2.8655	-6.0412	+1.4036	+6.0412
	(4-MRs)	-7.4763	-4.6632	+2.8131	+3.0817	-6.0698	+1.4066	+6.0698
$^{*}Mg_{17}^{-1}$— N_2	(8-MR)	-1.6879	+0.6111	+2.2990	-0.0043	-0.5384	+1.1495	+0.5384
	(4-MRs)	-1.6801	+0.7567	+2.4368	+5.9893	-0.4616	+1.2184	+0.4616
$^{**}Mg_{17}^{-1}$— N_2	(8-MR)	-1.8134	+0.6549	+2.4683	+0.0649	-0.5792	+1.2342	+0.5792
	(4-MRs)	-1.7910	+0.7349	+2.5259	+2.3999	-0.5280	+1.2630	+0.5280

$Mg_{16}Ca$— N_2	(8-MR)	-4.5525	-1.5764	+2.9761	+52.7458	-3.0644	+1.4881	+3.0644
	(4-MRs)	-4.5486	-1.5809	+2.9677	+52.3147	-3.0648	+1.4838	+3.0648

The * and ** show the spin-up case (Alfa MOs) and the spin-down case (Beta MOs), respectively

The chemical reactivity of the $Mg_{16}M$ nanoclusters can be characterized by their energy gap which is an important parameter relying on the HOMO and LUMO energy levels. The large energy gap indicates the high stability and consequently the low chemical reactivity, as such, a small gap represents the low stability and a high chemical reactivity [62-64]. Table 4 clearly shows that the $Mg_{16}Ca$ nanocluster has a smaller energy gap, low stability, and high chemical reactivity in comparison to the Mg_{17} and $Mg_{16}Be$ nanoclusters, which lead to more sensitivity to the presence of N_2 molecule. The dependency of the E_{gap} to the conduction electron population (N) based on equation (5), has been proven many times [65-67] and its alteration can be used as an appropriate index for the adsorbent sensitivity to a chemical.

$$N = A\,T^{3/2}\exp(-E_{gap}/2kT) \qquad (5)$$

where k is the Boltzmann's constant and A (electrons/m^3 $K^{3/2}$) is a constant.

Eq. 5 estimates an exponential increase for the electrical conductivity of the $Mg_{16}M$ by decreasing the E_{gap}. This alteration can be converted to an electrical signal, assisting to detect the molecule. Therefore, Eq. 5 predicts a decrease in the electrical conductivity of $Mg_{16}Ca$ —N_2 by increasing E_{gap}.

The resistance of a chemical species to alter its electronic configuration is called the chemical hardness, while electronic chemical potential illustrates the desire to escape the electron cloud [68-70]. Table 4, represents the values of the chemical hardness and electronic chemical potential for $Mg_{16}Ca$ —N_2 complex for the 8-MR (η=1.4881 and μ=-3.0644 eV) and 4-MRs frames (η=1.4838 and μ=-3.0648 eV). The comparison between these values with the values of $Mg_{16}Ca$ nanocluster (η=0.9742 and μ=-3.0801 eV) indicates a significant increase

in η and μ during the adsorption of N_2 molecule. Moreover, the values of the chemical hardness for $Mg_{16}Be$, Mg_{17}, and $Mg_{16}Ca$ are 1.5089 eV, 1.2981 eV, and 0.9742 eV, respectively. It seems that in the three different nanoclusters, the chemical hardness decreases with increasing the radius of the central atom. Accordingly, the $Mg_{16}Ca$ nanocluster represents the highest reactivity. The chemical potential values of the neutral and ionic magnesium nanoclusters $Mg_{17}^{q}(q=0,\pm1)$ show that the neutral nanocluster more stabilized by losing one electron while, accepting an electron causes instability in the resulting anionic nanocluster. It should be noted that the instability of the anionic nanocluster compared to the cationic one, does not lead to its high reactivity with N_2 molecule, because the presence of an empty orbital in the cationic nanocluster plays an effective role in the nucleophilic attack by the lone pair electrons of N_2 molecule. Accordingly, the N_2 molecule has better adsorption on the cationic cluster.

The values of the energy gap for $Mg_{16}Be$, Mg_{17}, and $Mg_{16}Ca$ nanoclusters are 3.0177 eV, 2.5960 eV and 1.9484 eV, respectively. These values indicated a reduction in the energy gap with increasing the radius of the central atom, which causes more instability and reactivity. Thus, $Mg_{16}Ca$ nanocluster with 1.9484 eV gap energy has the most reactivity to interaction with N_2 molecule, which confirmed with the results of the adsorption energy values in the section of 3.2. Moreover, each of the ionic magnesium nanoclusters $Mg_{17}^{q}(q=\pm1)$ with a doublet spin multiplicity $(S=2)$ has two different HOMO-LUMO energy gaps. The most value of the band gap, and consequently the most stability are related to the anionic (the spin-down case) and cationic (the spin-up case) nanoclusters, respectively (Figures 4 and 5).

In order to verify the effects of N_2 adsorption on the electronic properties of the magnesium nanoclusters, electronic densities of states (DOSs) of the molecule/nanoclusters

have been presented in Figures. SF5 and SF6, supplementary material. The examination of the DOS plots reveal that for the 8-MR frame of $Mg_{16}Be$ —N_2 and 4-MRs frames of Mg_{17}—N_2 complexes, the conduction levels shift toward the lower energies compared to those of their pristine nanoclusters, whereas for 4-MRs and 8-MR frames of $Mg_{16}Ca$ —N_2 and Mg_{17}^{+1}—N_2, and 4-MRs frames of Mg_{17}^{-1}—N_2 complexes, the conduction levels shift toward the higher energies. According to Figures. SF5 and SF6, supplementary material, for 4-MRs frame of $Mg_{16}Be$ —N_2 (a), 8-MR frame of Mg_{17}—N_2 (d), and 8-MR frame of Mg_{17}^{-1}—N_2 (k), the DOS plots do not show significant changes compared to that of the pristine nanocluster. Therefore, there is no change in the conductance of these nanoclusters based on the adsorption of N_2 molecule. While for the $Mg_{16}Ca$ —N_2 (4-MRs and 8-MR) complex (Figure. SF5, supplementary material, (e) and (f)) several new peaks appear within the energy gap near the conduction level which indicate the N_2 molecule has a stronger interaction with the $Mg_{16}Ca$ nanocluster. Moreover, there is an overlap between the partial density of state (PDOS) of the nanoclusters and the total density of state (TDOS) of the investigated complexes (Figures. SF7 and SF8, supplementary material). Hence, it can be concluded that the nanocluster has a significant contribution towards HOMO. In contrast, the LUMO level arises from the contribution of N_2 orbitals in the investigated complexes (Figures. SF7 and SF8, supplementary material).

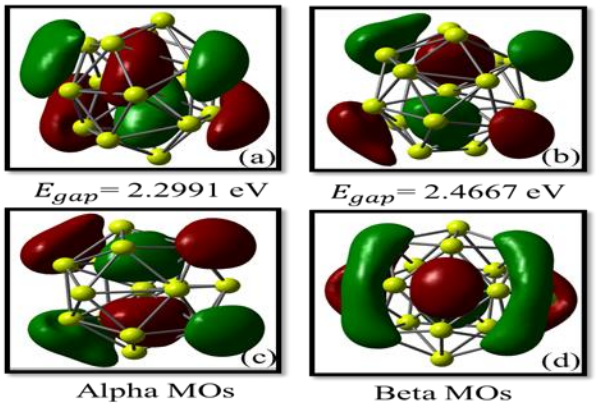

(a), (b) LUMO and (c), (d) HOMO profiles of the Mg_{17}^{-1} nanocluster.

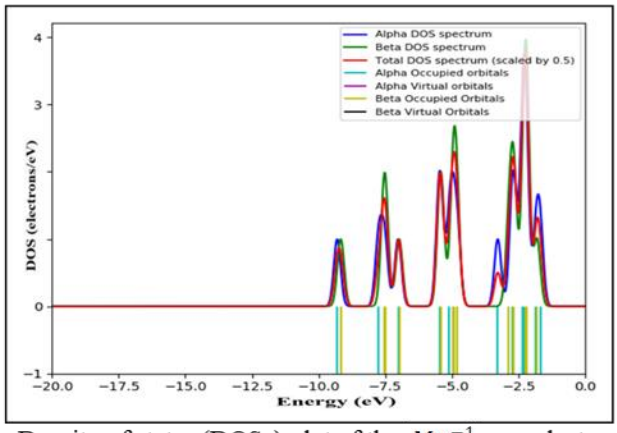

Density of states (DOSs) plot of the Mg_{17}^{-1} nanocluster.

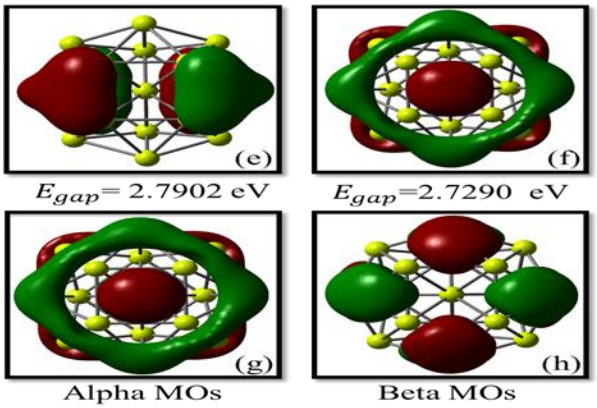

(e), (f) LUMO and (g), (h) HOMO profiles of the Mg_{17}^{+1} nanocluster.

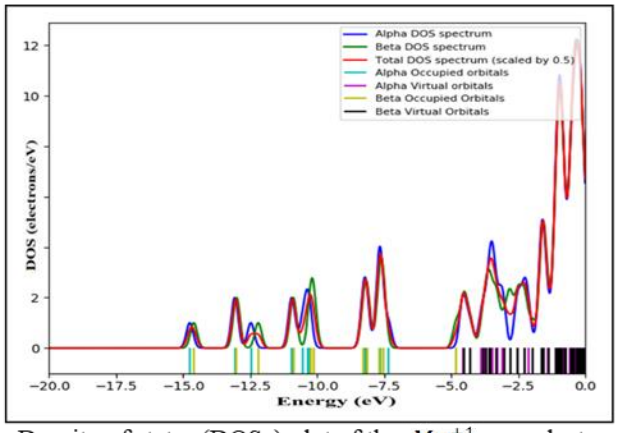

Density of states (DOSs) plot of the Mg_{17}^{+1} nanocluster.

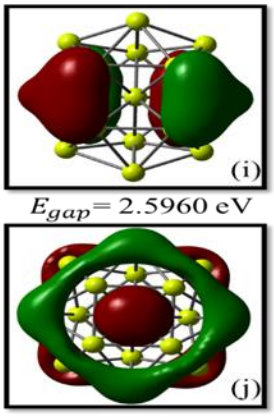

(i) LUMO and (j) HOMO profiles of the Mg_{17} nanocluster.

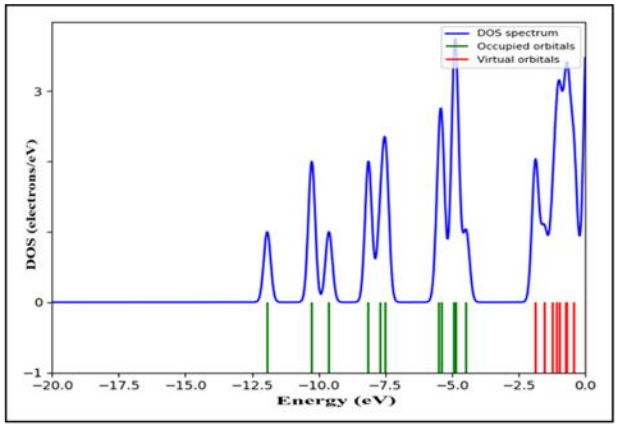

Density of states (DOSs) plot of the Mg_{17} nanocluster.

Figure. 4 The HOMO, LUMO, and DOS profiles of the neutral and ionic nanoclusters of Mg_{17}^{q} $(q = 0, \pm 1)$. The E_{gap} indicates the HOMO–LUMO energy gap.

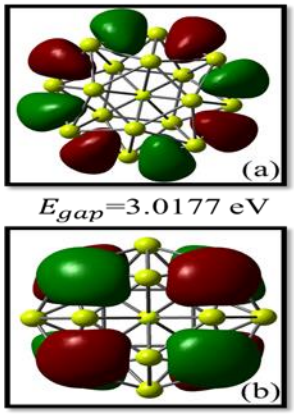

(a) LUMO and (b) HOMO profiles of the $Mg_{16}Be$ nanocluster.

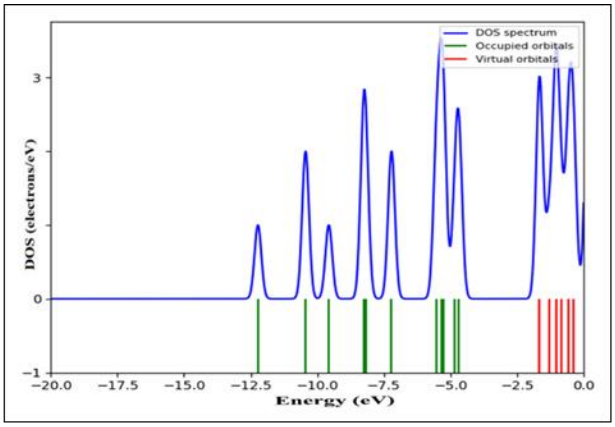

Density of states (DOSs) plot of the $Mg_{16}Be$ nanocluster.

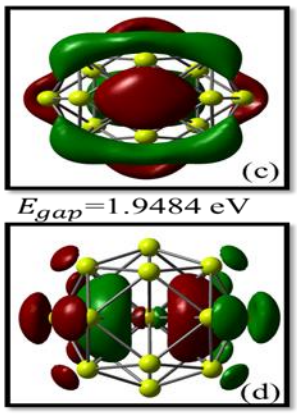

(c) LUMO and (d) HOMO profiles of the $Mg_{16}Ca$ nanocluster.

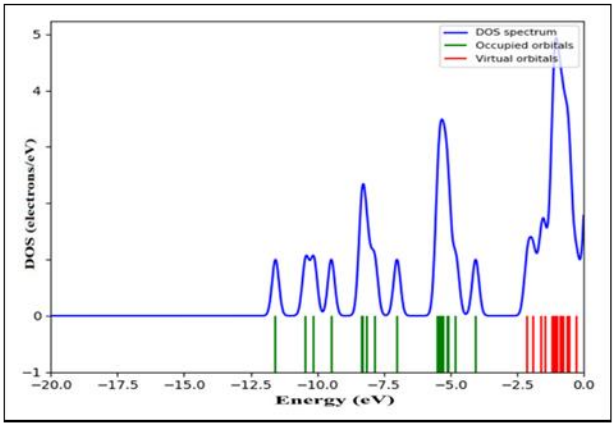

Density of states (DOSs) plot of the $Mg_{16}Ca$ nanocluster.

Figure. 5 The HOMO, LUMO, and DOS profiles of the neutral nanoclusters of $Mg_{16}M$ $(M = Be, Ca)$. The E_{gap} indicates the HOMO–LUMO energy gap.

3.4 Thermodynamic parameters

For more consideration of the N_2 adsorption process on the magnesium nanoclusters, the thermodynamic parameters such as standard enthalpy (ΔH°) and standard Gibbs free energy (ΔG°) at 298 K and 1 atmosphere were calculated based on the equation (6) and the results are tabulated in Table 5.

$$\Delta X^\circ = X\,(Mg_{16}M^q \ldots N_2) - \left(\, X_{Mg_{16}M^q} + X_{N_2} \right) \quad X = H, G \qquad (6)$$

Where $X_{Mg_{16}M^q\ldots N_2}$ ،$X_{Mg_{16}M^q}$ و X_{N_2} are thermodynamic parameters corresponding to the complex (nanocluster/N_2), nanocluster, and N_2 molecule respectively.

Table 5. The calculated thermodynamic properties; standard enthalpy (ΔH°), standard entropy ($T\Delta S^\circ$) and standard Gibbs free energy (ΔG°) all in (kJ.mol^{-1}) for the studied complexes at the CAM-B3LYP/6-311+G(d) level of theory.

Complexes	Metal ring frame	ΔH°	$T\Delta S^\circ$	ΔG°
$Mg_{17}^{-1} - N_2$		+0.4621	+16.1573	-15.6952
$Mg_{17}^{+1} - N_2$		+2.0741	+13.5948	-11.5207
$Mg_{16}Be - N_2$	8 –MR	-0.6774	+15.0887	-15.7661
$Mg_{17} - N_2$		+2.7463	+11.9381	-9.1919
$Mg_{16}Ca - N_2$		-86.5365	-65.6979	-20.8386
$Mg_{17}^{-1} - N_2$		+3.5786	+34.1420	-30.5635
$Mg_{17}^{+1} - N_2$		+1.4099	+15.8370	-14.4271
$Mg_{16}Be - N_2$	4-MRs	+2.6990	+13.9650	-11.2660
$Mg_{17} - N_2$		+2.1923	+15.8081	-13.6158
$Mg_{16}Ca - N_2$		-84.5727	-71.5817	-12.9909

The negative values of the standard enthalpy for $Mg_{16}Ca$ —N_2 (4-MRs and 8-MR frames) and $Mg_{16}Be$ —N_2 (8-MR) complexes indicated an exothermic reaction. The large negative values of $T\Delta S^\circ$ denote an entropy reduction during the formation of these complexes. The positive values of the standard Gibbs free energy for both 4-MRs and 8-MR frames of Mg_{17}^{+1}—N_2 , Mg_{17}^{-1}—N_2, $Mg_{16}Be$—N_2, and $Mg_{16}Be$ —N_2 complexes predicted a thermodynamically disfavored adsorption process for these complexes. The negative values of the standard Gibbs free energy for $Mg_{16}Ca$ —N_2 complex for both 4-MRs and 8-MR frames, verifying a spontaneous and thermodynamically favorable adsorption process which leads to an increase in the capability for N_2 storage. This results represent a linear correlation between adsorption energy and standard enthalpy of these complexes at the CAM-B3LYP approach with the corresponding correlation coefficient of 0.99 (Figure. SF9, supplementary

material). The $Mg_{16}Ca—N_2$ nanocluster with the E_{ad} = -87.617 (kJ.mol^{-1}) and ΔH°= -86.5365 (kJ.mol^{-1}) for 8-MR frame; and E_{ad} = -88.0620 (kJ.mol^{-1}) and ΔH°= -84.5727 (kJ.mol^{-1}) for 4-MR frames adsorbed N_2 molecule during a chemisorption reaction. These results are in line with available works [71].

4. Conclusions

The CAM-B3LYP/6-311+G(d) method was employed to investigate the interaction between the N_2 molecule with the $Mg_{16}M$ (*M=Be, Mg,* and *Ca*), *M* is the central atom, and also with $Mg_{17}^{q}(q = 0, \pm 1)$ nanoclusters in the gas phase. Based on the adsorption energies and enthalpies, a thermodynamically favorable adsorption process was predicted for the $Mg_{16}Ca—N_2$ complex. The negative value of the Gibbs free energy of $Mg_{16}Ca—N_2$ confirmed the spontaneous adsorption process. The highest interaction energy was observed for the $Mg_{16}Ca$ nanocluster at the 8-MR frame which causes a high charge transfer of 0.0711 e. Furthermore, the nitrogen molecule is chemisorbed on the $Mg_{16}Ca$ nanocluster while it retains its molecular form. The NBO analysis revealed that in all complexes, the nitrogen molecule is an electron-donating and the nanocluster is the electron acceptor. The nanocluster has a significant contribution towards HOMO whereas the LUMO level arises from the contribution of N_2 orbitals in the investigated complexes. The estimated recovery time for $Mg_{16}Ca—N_2$ complex was 0.075 s for 8-MR frame and 0.089 s for 4-MRs frames, which represented a possible desorption process for the N_2 molecule from the surface of $Mg_{16}Ca$. The conduction electron population (N) predicted a decrease in the electrical conductivity of $Mg_{16}Ca—N_2$ by increasing E_{gap}. These changes can be converted to an electrical signal, helping to detect the molecule. In summary, the $Mg_{16}Ca$ nanocluster may be a promising candidate for detection of N_2 molecule.We anticipate that the substitution of central *Mg* atom

with the divalent metal with a larger radius than *Mg* can increase the sensitivity of the aromatic metal $Mg_{16}M$ nanoclusters to use as a sensor for N_2 gas.

References:

[1] N. N. Greenwood, Earnshaw, A. Chemistry of the Elements. 2nd ed. Amesterdam, Elsevier 1997.

[2] Bose, R.K. Nitrogen inerting system for explosion prevention in aircraft fuel tank and oxygenating system for improving combustion efficiency of aerospace rockets/aircraft engines. Google Patents, 2010.

[3] Kasyutich, V., Bale, C., Canosa-Mas, C., Pfrang, C., Vaughan, S., Wayne, R. Cavity-enhanced absorption: detection of nitrogen dioxide and iodine monoxide using a violet laser diode. Appl. Phys. B. 2003, 76, 691-7.

[4] Simmons, J. Overview: high-nitrogen alloying of stainless steels. Mater. Sci. Eng. A. 1996, 207, 159-69.

[5] Kuypers, M.M., Marchant, H.K., Kartal, B. The microbial nitrogen-cycling network. Nat. Rev. Microbiol. 2018, 16, 263.

[6] Tracey, W.R. Spectrophotometric detection of nitrogen oxides using azo dyes. Neuroprotocols. 1992, 1, 125-31.

[7] Sun, W., Dong, L., Lu, Y., Deng, Y., Yu, J., Sun, X., et al. Electrochemical detection of rutin on nitrogen-doped graphene modified carbon ionic liquid electrode. Sens. Actuators B Chem. 2014, 199, 36-41.

[8] Huber, S.A., Balz, A., Abert, M., Pronk, W. Characterisation of aquatic humic and non-humic matter with size-exclusion chromatography–organic carbon detection–organic nitrogen detection (LC-OCD-OND). Water Res. 2011, 45, 879-85.

[9] Noh JS, Lee JM, W., L. Low-dimensional palladium nanostructures for fast and reliable hydrogen gas detection. . Sensors (Basel). 2011, 11, 825-51.

[10] Hadipour, N.L., Ahmadi Peyghan, A., Soleymanabadi, H. Theoretical Study on the Al-Doped ZnO Nanoclusters for CO Chemical Sensors. J Phys Chem C. 2015, 119, 6398-404.

[11] Vessally, E., Siadati, S.A., Hosseinian, A., Edjlali, L. Selective sensing of ozone and the chemically active gaseous species of the troposphere by using the C20 fullerene and graphene segment. Talanta. 2017, 162, 505-10.

[12] Beheshtian, J., Peyghan, A.A., Bagheri, Z. Selective function of Al12N12 nano-cage towards NO and CO molecules. Comput Materials Sci. 2012, 62, 71-4.

[13] Bagheri, Z., Peyghan, A.A. DFT study of NO2 adsorption on the AlN nanocones. Comput Theor Chem. 2013, 1008, 20-6.

[14] Bahrami, A., Seidi, S., Baheri, T., Aghamohammadi, M. A first-principles study on the adsorption behavior of amphetamine on pristine, P-and Al-doped B12N12 nano-cages. Superlattices Microstruct. 2013, 64, 265-73.

[15] Wang, H. A density functional investigation of fluorinated B12N12 clusters. Chin. J. Chem. 2010, 28, 1897-901.

[16] Nakazawa, T., Igarashi, T., Tsuru, T., Kaji, Y. Ab initio calculations of Fe–Ni clusters. Comput. Mater. Sci. 2009, 46, 367-75.

[17] Jellinek, J., Acioli, P.H. Magnesium clusters: structural and electronic properties and the size-induced nonmetal-to-metal transition. J. Phys. Chem. A. 2002, 106, 10919-25.

[18] Heidari, I., De, S., Ghazi, S., Goedecker, S., Kanhere, D. Growth and Structural Properties of Mg N (N= 10–56) Clusters: Density Functional Theory Study. J. Phys. Chem. A. 2011, 115, 12307-14.

[19] Janecek, S., Krotscheck, E., Liebrecht, M., Wahl, R. Structure of Mg n and Mg n+ clusters up to n= 30. Eur. Phys. J. D. 2011, 63, 377-90.

[20] Köhn, A., Weigend, F., Ahlrichs, R. Theoretical study on clusters of magnesium. Phys. Chem. Chem. Phys. 2001, 3, 711-9.

[21] Lyalin, A., Solov'yov, I.A., Solov'yov, A.V., Greiner, W. Evolution of the electronic and ionic structure of Mg clusters with increase in cluster size. Phys. Rev. A. 2003, 67, 063203-15.

[22] Monteverde, M., Nunez-Regueiro, M., Rogado, N., Regan, K., Hayward, M., He, T., et al. Pressure dependence of the superconducting transition temperature of magnesium diboride. Science. 2001, 292, 75-7.

[23] Er, S., de Wijs, G.A., Brocks, G. Tuning the hydrogen storage in magnesium alloys. J. Phys. Chem. Lett. 2010, 1, 1982-6.

[24] Nevshupa, R., Ares, J.R., Fernández, J.F., del Campo, A., Roman, E. Tribochemical decomposition of light ionic hydrides at room temperature. J. Phys. Chem. Lett. 2015, 6, 2780-5.

[25] Barcaro, G., Ferrando, R., Fortunelli, A., Rossi, G. Exotic supported copt nanostructures: from clusters to wires. J. Phys. Chem. Lett. 2009, 1, 111-5.

[26] Chen, L.-Y., Xu, J.-Q., Choi, H., Pozuelo, M., Ma, X., Bhowmick, S., et al. Processing and properties of magnesium containing a dense uniform dispersion of nanoparticles. Nature. 2015, 528, 539-43.

[27] Yoo, J., Aksimentiev, A. Improved parametrization of Li+, Na+, K+, and Mg2+ ions for all-atom molecular dynamics simulations of nucleic acid systems. J. Phys. Chem. Lett. 2011, 3, 45-50.

[28] Jellinek, J., Acioli, P.H. Magnesium Clusters: Structural and Electronic Properties and the Size-Induced Nonmetal-to-Metal Transition. J. Phys. Chem. A. 2003, 107, 1670-.

[29] Akola, J., Rytkönen, K., Manninen, M. Metallic evolution of small magnesium clusters. Eur. Phys. J. D. 2001, 16, 21-4.

[30] Davidson, E.R., Frey, R.F. Density functional calculations for Mg n+ clusters. J. Chem. Phys. 1997, 106, 2331-41.

[31] Gong, X., Zheng, Q., He, Y.-z. Electronic structures of magnesium clusters. Phys. Lett. A. 1993, 181, 459-64.

[32] Kumar, V., Car, R. Structure, growth, and bonding nature of Mg clusters. Phys. Rev. B. 1991, 44, 8243-55.

[33] Xia, X., Kuang, X., Lu, C., Jin, Y., Xing, X., Merino, G., et al. Deciphering the structural evolution and electronic properties of magnesium clusters: an aromatic homonuclear metal Mg17 cluster. J. Phys. Chem. A. 2016, 120, 7947-54.

[34] Jellinek, J., Acioli, P.H. Magnesium Clusters: Structural and Electronic Properties and the Size-Induced Nonmetal-to-Metal Transition. J Phys Chem A. 2002, 106, 10919-25.

[35] Lyalin, A., Solov'yov, I.A., Solov'yov, A.V., Greiner, W. Evolution of the electronic and ionic structure of Mg clusters with increase in cluster size. Phys Rev A. 2003, 67, 063203.

[36] Jiao, Y., Du, A., Zhu, Z., Rudolph, V., Smith, S.C. A density functional theory study of CO 2 and N 2 adsorption on aluminium nitride single walled nanotubes. J. Mater. Chem. 2010, 20, 10426-30.

[37] Jiao, Y., Du, A., Zhu, Z., Rudolph, V., Smith, S.C. Adsorption of carbon dioxide and nitrogen on single-layer aluminum nitride nanostructures studied by density functional theory. J. Phys. Chem. C. 2010, 114, 7846-9.

[38] Cortés-Arriagada, D., Villegas-Escobar, N. A DFT analysis of the adsorption of nitrogen oxides on Fe-doped graphene, and the electric field induced desorption. APPL SURF SCI. 2017, 420, 446-55.

[39] Gamallo, P., Sayós, R. A density functional theory study of atomic oxygen and nitrogen adsorption over α-alumina (0001). Phys. Chem. Chem. Phys. 2007, 9, 5112-20.

[40] Al-Abadleh, H.A., Grassian, V. FT-IR study of water adsorption on aluminum oxide surfaces. Langmuir. 2003, 19, 341-7.

[41] Chen, J.-K., Yang, S.-M., Li, B.-H., Lin, C.-H., Lee, S. Fluorescence quenching investigation of methyl red adsorption on aluminum-based metal–organic frameworks. Langmuir. 2018, 34, 1441-6.

[42] Kuang, X.-J., Wang, X.-Q., Liu, G.-B. A density functional study on the adsorption of hydrogen molecule onto small copper clusters. J. Chem. Sci. 2011, 123, 743-54.

[43] Ma, Q.-M., Xie, Z., Wang, J., Liu, Y., Li, Y.-C. Structures, binding energies and magnetic moments of small iron clusters: A study based on all-electron DFT. Solid State Commun. 2007, 142, 114-9.

[44] Hussain, R., Hussain, A.I., Chatha, S.A.S., Mansha, A., Ayub, K. Density functional theory study of geometric and electronic properties of full range of bimetallic AgnYm (n+ m= 10) clusters. J. Alloys Compd. 2017, 705, 232-46.

[45] Matar, S.F. DFT study of hydrogen instability and magnetovolume effects in CeNi. Solid State Sci. 2010, 12, 59-64.

[46] Weinhold, F., Landis, C.R. Natural bond orbitals and extensions of localized bonding concepts. Chemistry Education Research and Practice. 2001, 2, 91-104.

[47] Dennington, R.D., Keith, T.A., Millam, J.M. GaussView 5.0. 8. Gaussian Inc. 2008, 340.

[48] Yanai, T., Tew, D.P., Handy, N.C. A new hybrid exchange–correlation functional using the Coulomb-attenuating method (CAM-B3LYP). Chem. Phys. Lett. 2004, 393, 51-7.

[49] Lee, C., Yang, W., Parr, R.G. Development of the Colle-Salvetti correlation-energy formula into a functional of the electron density. Phys. Rev. B. 1988, 37, 785-9.

[50] Frisch, M., Trucks, G., Schlegel, H.B., Scuseria, G., Robb, M., Cheeseman, J., et al. Gaussian 09, Revision B.01. Gaussian, Inc., Wallingford, CT, 2009.

[51] Boys, S.F., Bernardi, F. The calculation of small molecular interactions by the differences of separate total energies. Some procedures with reduced errors. Mol. Phys. 1970, 19, 553-66.

[52] O'Boyle, N.M., Tenderholt, A.L., Langner, K.M. cclib: A library for package-independent computational chemistry algorithms. J Comput Chem. 2008, 29, 839-45.

[53] Lu, T., Chen, F. Multiwfn: A multifunctional wavefunction analyzer. J Comput Chem. 2012, 33, 580-92.

[54] Huber, K.-P. Molecular spectra and molecular structure: IV. Constants of diatomic molecules, Springer Science & Business Media, 2013.

[55] Johnson III, R.D. NIST Computational Chemistry Comparison and Benchmark Database, NIST Standard Reference Database Number 101, Release 12, Aug 2005. Johnson III http://srdata. nist. gov/cccbdb. 2005.

[56] Shahabi, M., Raissi, H. Molecular dynamics simulation and quantum chemical studies on the investigation of aluminum nitride nanotube as phosgene gas sensor. J Incl Phenom Macrocycl Chem. 2016, 86, 305-22.

[57] Hosseinian, A., Vessally, E., Bekhradnia, A., Ahmadi, S., Nezhad, P.D.K. Interaction of α-cyano-4-hydroxycinnamic acid drug with inorganic BN nanocluster: A density functional study. J Inorg Organomet Polym Mater. 2018, 28, 1422-31.

[58] Vessally, E., Behmagham, F., Massuomi, B., Hosseinian, A., Nejati, K. Selective detection of cyanogen halides by BN nanocluster: a DFT study. J. Mol. Model. 2017, 23, 138.

[59] Nejati, K., Hosseinian, A., Vessally, E., Bekhradnia, A., Edjlali, L. A comparative DFT study on the interaction of cathinone drug with BN nanotubes, nanocages, and nanosheets. Appl. Surf. Sci. 2017, 422, 763-8.

[60] Wang, H., Maiyalagan, T., Wang, X. Review on recent progress in nitrogen-doped graphene: synthesis, characterization, and its potential applications. Acs Catalysis. 2012, 2, 781-94.

[61] Ahmadi, S., Achari, V.M., Nguan, H., Hashim, R. Atomistic simulation studies of the α/β-glucoside and galactoside in anhydrous bilayers: effect of the anomeric and epimeric configurations. J. Mol. Model. 2014, 20, 2165.

[62] Pearson, R.G. Absolute electronegativity and hardness: applications to organic chemistry. J. Org. Chem. 1989, 54, 1423-30.

[63] Zhou, Z., Parr, R.G. Activation hardness: new index for describing the orientation of electrophilic aromatic substitution. J. Am. Chem. Soc. 1990, 112, 5720-4.

[64] Faust, W. Explosive molecular ionic crystals. Science. 1989, 245, 37-42.

[65] Ahmadi Peyghan, A., Hadipour, N.L., Bagheri, Z. Effects of Al doping and double-antisite defect on the adsorption of HCN on a BC2N nanotube: density functional theory studies. J. Phys. Chem. C. 2013, 117, 2427-32.

[66] Eslami, M., Vahabi, V., Peyghan, A.A. Sensing properties of BN nanotube toward carcinogenic 4-chloroaniline: a computational study. Physica E: Low-dimensional Systems and Nanostructures. 2016, 76, 6-11.

[67] Samadizadeh, M., Peyghan, A.A., Rastegar, S.F. Sensing behavior of BN nanosheet toward nitrous oxide: a DFT study. CHINESE CHEM LETT. 2015, 26, 1042-5.

[68] Parr, R.G., Pearson, R.G. Absolute hardness: companion parameter to absolute electronegativity. J. Am. Chem. Soc. 1983, 105, 7512-6.

[69] Parr, R.G., Chattaraj, P.K. Principle of maximum hardness. J. Am. Chem. Soc. 1991, 113, 1854-5.

[70] Pearson, R.G. Absolute electronegativity and absolute hardness of Lewis acids and bases. J. Am. Chem. Soc. 1985, 107, 6801-6.

[71] Mosapour Kotena, Z., Behjatmanesh–Ardakani, R., Hashim, R. The interaction between sugar-based surfactant with zigzag single-walled carbon nanotubes: insight from a computational study. Liq Crys. 2015, 42, 158-66.